



HHS Public Access

Author manuscript

Acta Neuropathol. Author manuscript; available in PMC 2022 February 01.

Published in final edited form as:

Acta Neuropathol. 2021 February ; 141(2): 303–321. doi:10.1007/s00401-020-02256-1.

Multi-omic molecular profiling reveals potentially targetable abnormalities shared across multiple histologies of brain metastasis

Kazutaka Fukumura¹, Prit Benny Malgulkar¹, Grant M. Fischer^{1,2,3}, Xiaoding Hu⁴, Xizeng Mao⁵, Xingzhi Song⁵, Sharia D. Hernandez¹, Xiang H.-F. Zhang^{6,7,8,9}, Jianhua Zhang⁵, Edwin Roger Parra¹, Dihua Yu^{10,11}, Bisrat G. Debeb⁴, Michael A. Davies^{1,3,12}, Jason T. Huse^{1,13,*}

¹Department of Translational Molecular Pathology, the University of Texas MD Anderson Cancer Center, Houston, TX 77030, USA

²Department of Cancer Biology, the University of Texas MD Anderson Cancer Center, Houston, TX 77030, USA

³Department of Melanoma Medical Oncology, the University of Texas MD Anderson Cancer Center, Houston, TX 77030, USA

⁴Department of Breast Medical Oncology, the University of Texas MD Anderson Cancer Center, Houston, TX 77030, USA

⁵Department of Genomic Medicine, the University of Texas MD Anderson Cancer Center, Houston, TX 77030, USA

⁶Lester and Sue Smith Breast Center, Baylor College of Medicine, Houston, TX 77030, USA

⁷Dan L. Duncan Cancer Center, Baylor College of Medicine, Houston, TX 77030, USA

⁸Department of Molecular and Cellular Biology, Baylor College of Medicine, Houston, TX 77030, USA

⁹McNair Medical Institute, Baylor College of Medicine, Houston, TX 77030, USA

¹⁰Department of Molecular and Cellular Oncology, the University of Texas MD Anderson Cancer Center, Houston, TX 77030, USA

Terms of use and reuse: academic research for non-commercial purposes, see here for full terms. <https://www.springer.com/aam-terms-v1>

*Corresponding author. JHuse@mdanderson.org. Phone: 713-745-3186, FAX: 713-745-8221.

Author contributions K.F. and J.T.H. conceptualized the study and designed the experiments. K.F., P.B.M., G.M.F., X.H., X.M., X.S., X.H.-F.Z., J.Z., S.D.H., E.R.P., D.Y., B.G.D., M.A.D., and J.T.H. performed the experiments and/or analyzed data. J.T.H. supervised the study. K.F., P.B.M., E.R.P., B.G.D., M.A.D., and J.T.H. wrote and/or revised the manuscript. All authors reviewed the manuscript.

Compliance with ethical standards

Conflict of interest M.A.D. receives commercial research grants from AstraZeneca, Roche/Genentech, GlaxoSmithKline, Myriad, Oncothyreon, and Sanofi-Aventis and is a consultant/advisory board member for GlaxoSmithKline, Novartis, Roche/Genentech, Array, Bristol-Myers Squibb, Sanofi-Aventis, Vaccinex, Syndax, and NanoString. All other authors declare no conflict of interest.

Publisher's Disclaimer: This Author Accepted Manuscript is a PDF file of an unedited peer-reviewed manuscript that has been accepted for publication but has not been copyedited or corrected. The official version of record that is published in the journal is kept up to date and so may therefore differ from this version.

¹¹MD Anderson Cancer Center UTHealth Graduate School of Biomedical Sciences, Houston, TX 77030, USA

¹²Department of Systems Biology, the University of Texas MD Anderson Cancer Center, Houston, TX 77030, USA

¹³Department of Pathology, the University of Texas MD Anderson Cancer Center, Houston, TX 77030, USA

Abstract

The deadly complication of brain metastasis (BM) is largely confined to a relatively narrow cross section of systemic malignancies, suggesting a fundamental role for biological mechanisms shared across commonly brain metastatic tumor types. To identify and characterize such mechanisms, we performed genomic, transcriptional, and proteomic profiling using whole-exome sequencing, mRNA-seq and reverse phase protein array analysis in a cohort of lung, breast, and renal cell carcinomas consisting of BM and patient-matched primary or extracranial metastatic tissues. While no specific genomic alterations were associated with BM, correlations with impaired cellular immunity, upregulated oxidative phosphorylation (OXPHOS), and canonical oncogenic signaling pathways including phosphoinositide 3-kinase (PI3K) signaling, were apparent across multiple tumor histologies. Multiplexed immunofluorescence analysis confirmed significant T cell depletion in BM, indicative of a fundamentally altered immune microenvironment. Moreover, functional studies using in vitro and in vivo modeling demonstrated heightened oxidative metabolism in BM along with sensitivity to OXPHOS inhibition in murine BM models and brain metastatic derivatives relative to isogenic parentals. These findings demonstrate that pathophysiological rewiring of oncogenic signaling, cellular metabolism, and immune microenvironment broadly characterizes BM. Further clarification of this biology will likely reveal promising targets for therapeutic development against BM arising from a broad variety of systemic cancers.

Keywords

Brain metastasis; Multiple histologies; Molecular profiling; Immunosuppression; Oxidative phosphorylation; Phosphoinositide 3-kinase (PI3K) signaling

Introduction

Brain metastasis (BM) is a frequent and deadly complication of systemic malignancy, occurring in 10–30% of adults with cancer [46]. Inherent limitations to surgical access and drug penetration within the central nervous system (CNS) further complicate the management of BM [20], and are rendered all the more clinically relevant by continued improvements in the treatment of disseminated malignancies at primary or other extracranial sites. BM most commonly occurs in a relatively narrow cross section of tumors, consisting primarily of lung, breast, and renal cell carcinomas along with malignant melanoma [4]; and while BM does feature in other neoplasms, its notable frequency in these specific contexts points to the possibility of shared underlying biological mechanisms driving migration to, colonization of, and/or growth within the unique CNS microenvironment.

Extensive genomic analyses performed on large sets of BMs and patient-matched primary tumors have revealed striking and clinically relevant heterogeneity with regard to mutation and copy number events [7, 21, 39]. However, these studies have yet to demonstrate specific genetic abnormalities driving BM in multiple tumor histologies, and shared BM-promoting pathways across different cancers remain unclear. A broad spectrum of biological pathways has been shown to influence BM in the context of single tumor types and/or experimental models, involving cell adhesion molecules, chemokines, extracellular matrix components and metalloproteinases, and microenvironmental constituents [36]. Of note, upregulated phosphoinositide 3-kinase (PI3K) signaling is a recurrent feature of melanoma BM [12, 16, 31]. Nevertheless, the extent to which this and other molecular abnormalities characterize brain metastatic neoplasms more generally is unknown.

Cellular and molecular drivers of BM are likely influenced by the unique microenvironmental characteristics of the CNS [26]. Intrinsic factors, including the blood-brain barrier, serve to maintain an “immune privileged” state within the brain and spinal cord, featuring minimal surveillance from peripherally derived immune cells [37]. Moreover, the specific physiological, microvascular, and cellular properties of the CNS apply nutritional and metabolic constraints to any cellular constituent, whether normal or pathological. These include high levels of lipids, particularly polyunsaturated fatty acids, dynamic glucose and oxygen consumption, and segregated anaerobic and aerobic metabolism in astrocytes and neurons, respectively [24, 44]. Recent work from our group demonstrated that significant immunosuppression and upregulated oxidative phosphorylation (OXPHOS) featured prominently in melanoma BM [21]. The extent to which these abnormalities characterized BM more broadly has not been extensively explored.

To identify shared cellular and molecular factors driving BM across distinct primary tumor histologies, we performed genomic, transcriptional, and proteomic profiling in a cohort of lung, breast, and renal cell carcinomas consisting of both BMs and patient-matched primary or extracranial metastatic tissues (P/EMs). As in prior studies, BMs were characterized by notable genomic heterogeneity, pointing towards idiosyncratic pathways of molecular evolution. Consistent with earlier work in melanoma, we demonstrated elevated PI3K pathway signaling as a generalizable feature across different BM histologies, along with relative immunosuppression and enhanced OXPHOS. Detailed morphological analysis revealed significant T cell depletion in BMs, indicative of impaired cellular immunity in the tumor microenvironment. Finally, a central role for OXPHOS in BM was confirmed using *in vitro* and *in vivo* disease models. Taken together, our findings reveal that oncogenic signaling, metabolism, and immune microenvironment abnormalities are shared across multiple histologies of BM, and may be amenable to therapeutic targeting.

Materials and Methods

Clinical specimens

This study was approved by Institutional Review Board of the University of Texas MD Anderson Cancer Center (MDACC), and all surgically resected normal or tumor tissues and patient-matched white blood cells were collected at MDACC with written informed consent

from their respective patients. Specimen quality control was conducted by a board-certified Neuropathologist (J.T.H.) and the following profiling analyses were performed using tissues with at least 70% viable tumor content. A total of 35 patients with matched P/EM and BM tissues from breast ($N=14$), lung ($N=14$) and renal cell ($N=7$) carcinomas were available for this study. Two lung cancer patients provided two distinct BM samples, respectively (Supplementary Table 1, online resource). 33 FFPE samples were also collected, consisting of primary tumors or BMs from breast (primary tumor, $N=2$; BM, $N=4$), lung (primary tumor, $N=7$; BM, $N=10$) and renal cell carcinomas (primary tumor, $N=4$; BM, $N=6$). Overlap with our frozen tissue sample set consisted of 9 primary tumors and 16 BMs, reflecting 8 patient-matched cases along with additional unmatched tissues.

DNA and RNA extraction

DNA and RNA from frozen tissues were extracted with AllPrep DNA/RNA/miRNA Universal kits (Qiagen), and DNA from white blood cells was isolated with QIAamp DNA Mini kits (Qiagen). Biomaterial concentration was measured with a Qubit 3.0 fluorometer (Thermo Fisher Scientific), and RNA quality was evaluated using the 2200 TapeStation System (Agilent).

Whole-exome sequencing

Genomic DNA was enriched for exonic fragments using the SureSelect Human All Exon V6 + COSMIC approach (Agilent), followed by massively parallel sequencing on the HiSeq4000 platform (Illumina) using a 75-bp paired-end option. BCL files were processed using Illumina's Consensus Assessment of sequence And Variation (CASAVA) tool for demultiplexing/conversion to FASTQ format. FASTQ files were then aligned to the human reference genome (hg19) using BWA-MEM [28] with 31 bp seed length. Aligned BAM files were then subjected to mark duplication, re-alignment, and re-calibration using Picard and GATK [18]. For downstream analysis, BAM files were subjected to germline mutation calls using Platypus [38], somatic mutation calls using MuTect [15], and indel calls using Pindel [48]. Genotyping quality checks were conducted assessing germline single-nucleotide polymorphisms (SNPs), and overlapping percentages of SNPs were calculated between patient-matched specimens. All samples were authenticated to pass the quality check with no swapping or contamination. DNA copy number analysis was conducted using the in-house application ExomeLyzer [50], followed by Circular Binary Segmentation [32]. Segmentation files were then loaded onto the Integrative Genomics Viewer [40] for visualization of copy number gains and losses. Frequently altered genes (> 10% of cohort) for breast, lung and renal cell carcinomas in the cBIOportal, ICGC and COSMIC databases were analyzed with our cohort and visualized using Oncoprint (<https://www.cbioportal.org>).

mRNA-seq

mRNA-seq was performed at MDACC Advanced Technology Genomics Core Facility. Libraries were prepared with the KAPA Stranded mRNA-seq kit (Kapa Biosystems) and sequenced on the Illumina HiSeq4000 platform using the 75-bp paired-end option. The sequencing data were converted to FASTQ format using Illumina bcl2fastq software. FASTQ reads were aligned to the human reference genome (hg19) using STAR [19] and further processed by Picard (v1.112) for marking duplicated reads. Raw read counts for each

gene were generated by HTSeq (v0.6.1) [3], and RPKM (Reads Per Kilobase Million) values were then calculated using in R (v3.2). Counts were normalized using the TMM method, and MDS plots were constructed with functions from the edgeR Bioconductor packages in R. Genes expressing low CPM counts were filtered using a \log_2 -(CPM >1 per sample) cutoff. Differentially expressed genes were defined using a Benjamini-Hochberg corrected P value less than 0.05. An analogous analysis pipeline was performed for the publicly available GEO data (GSE43837). GSEA was performed using the standard analysis pipeline with the Preranked module, and single sample GSEA (ssGSEA) was conducted on TMM-normalized, voom-transformed \log_2 -(CPM >1 per sample) expression matrices using the GenePattern module ssGSEA (v10.0.3) with default settings.

Reverse phase protein array (RPPA) assay

RPPA analysis was performed on proteins extracted from fresh frozen tissues at the MDACC RPPA Core Facility. In brief, proteins were isolated using lysis buffer (1% Triton X-100, 50mM HEPES, pH 7.4, 150mM NaCl, 1.5mM MgCl₂, 1mM EGTA, 100mM NaF, 10mM Na pyrophosphate, 1mM Na₃VO₄, 10% glycerol) containing freshly added protease and phosphatase inhibitors (Roche Applied Science), and arrayed on nitrocellulose-coated slides. Sample spots were then probed with 443 antibodies (<https://www.mdanderson.org/research/research-resources/core-facilities/functional-proteomics-rppa-core/antibody-information-and-protocols.html>) using a tyramide-based signal amplification approach and visualized by a 3,3'-diaminobenzidine (DAB) colorimetric reaction to produce stained slides. Stained slides were then scanned on a TissueScope scanner (Huron Digital Pathology) and densities quantified by Array-Pro Analyzer (v6.3). Differentially expressed proteins were obtained using WebMeV (Multiple Experiment Viewer; <http://mev.tm4.org/>), and pathway analyses were performed using Enrichr (<http://amp.pharm.mssm.edu/Enrichr/>).

Immune signature analysis

ESTIMATE and MCP-counter analyses were performed to determine the immune composition as previously described [5, 49]. mRNA-seq data were applied to TMM-normalized, voom-transformed \log_2 -(CPM >1 per sample) expression matrices. ESTIMATE produced the scores for stromal and immune compartments and the combined scores as “ESTIMATE score”, while MCP-counter determined the abundance scores for T cells, CD8 T cells, cytotoxic lymphocytes, NK cells, B lineage, monocytic lineage, myeloid dendritic cells, neutrophils, endothelial cells and fibroblasts.

Immunofluorescence

Multiplex immunofluorescence staining was performed as previously described [34]. Briefly, FFPE sections were subjected to primary antibodies for CD3 (Dako), CD8 (Thermo Fisher Scientific), granzyme B (Leica Biosystems), CD45RO (Leica Biosystems), FOXP3 (Cell Signaling Technology) and pancytokeratin AE1/AE3 (Dako), followed by imaging and scanning using the Vectra 3.0 multispectral imaging system (Akoya Biosciences) according to previously published instructions [33]. Scanning data were then assessed and quantified using the cell segmentation and phenotype tool by InForm 2.2.8 image analysis software (Akoya Biosciences) under pathologist supervision. Specific T cell subsets were determined as follows; total T cells, CD3+; cytotoxic T cells, CD3+ CD8+; cytotoxic T cells activated,

CD3+ CD8+ granzyme B+; memory T cells, CD3+ CD45RO+; effector/memory cytotoxic T cells, CD3+ CD8+ CD45RO+; regulatory T cells, CD3+ FOXP3+ CD8-; memory/regulatory T cells, CD3+ CD45RO+ FOXP3+.

Survival analysis

Patients with BMs were dichotomized into the high and low groups based on the quartiles of abundance scores for T cells, CD8 T cells or cytotoxic lymphocytes derived from MCP-counter analysis. Overall survival was determined using the time interval from date of craniotomy to the date of death or censoring. Survival outcome was analyzed by the Kaplan–Meier method and the survival curves drawn in GraphPad Prism 8.0.

OP-index

OXPPOS and the related pathway from MSigDB hallmark, curated and Gene Ontology (GO) gene sets in ssGSEA data (HALLMARK_OXIDATIVE_PHOSPHORYLATION, KEGG_OXIDATIVE_PHOSPHORYLATION, GO_OXIDATIVE_PHOSPHORYLATION, GO_REGULATION_OF_OXIDATIVE_PHOSPHORYLATION) were used to determine OP-index based on previously published methodology [21].

Cell culture

MDA-MB-231 parental cells were purchased from American Type Culture Collection (ATCC). MDA-MB-231-BR3, BT474 parental and -BR3 lines, and MDA-IBC3 cell lines were kindly provided by X.Z., D.Y. and B.D., respectively. MDA-MB-231 and BT474 cell lines were cultured in Dulbecco's Modified Eagle Medium (DMEM) high glucose (Gibco) and DMEM/F12 (Gibco), respectively, with 10% Fetal Bovine Serum (FBS, ATCC). MDA-IBC3 was cultured in Ham's F-12 Nutrient Mix (Gibco) with 10% FBS (Gibco), 5 µg/ml Insulin (Gibco) and 1 µg/ml Hydrocortisone (Sigma-Aldrich). Paired cell lines were authenticated using short tandem repeat DNA profiling at the MDACC Cytogenetics and Cell Authentication Core. All cell lines were routinely tested for mycoplasma using Universal Mycoplasma Detection Kit (ATCC).

Cell viability assays

Cells were plated at the density of 10,000 or 25,000 cells per well in 96-well plates. 24 hours later, the cells were treated with 0.5% methyl cellulose (Sigma-Aldrich) as vehicle control or IACS-10759 (Institute for Applied Cancer Sciences, MDACC) by substituting culture medium with medium containing the respective compound. Cell viability was determined 24 or 48 hours post treatment with four wells per condition by CellTiter-Glo (Promega), and normalized with values from vehicle control. Luminescence was measured using a FLUOstar Omega plate reader (BMG LABTECH).

Apoptosis assays

Apoptosis assays were performed using the Dead Cell Apoptosis Kit with Annexin V FITC and PI (Invitrogen). Cells were seeded in triplicate at the same density used for cell viability assays in 6-well plates and treated with vehicle or IACS-10759. Cells were harvested after incubation for 48 or 72 hours, and prepared for detection of apoptotic cells according to

manufacturer's instructions. Flow cytometric analysis was conducted using a BD Accuri C6 Flow Cytometer (BD Biosciences). Apoptotic cells were defined as propidium iodide (PI)-negative and Annexin V-positive, and the percentage of apoptotic cells induced by IACS-10759 was normalized to that of vehicle control.

Mitochondrial respiration analysis

Oxygen consumption rate (OCR) was determined using Seahorse XFe96 Analyzer (Agilent). Cells were plated at 20,000–30,000 cells per well in quintuplicate per condition. 12 hours later, medium was replaced with vehicle or 40nM IACS-10759-containing medium, and then exchanged with reconstituted Seahorse XF DMEM medium with 2.5mM Glucose and 1.0mM Glutamine (all from Agilent) 12 hours post treatment. The cells were incubated for 1 hour at 37 °C in a CO₂-free incubator before OCR measurement. With the Seahorse XF Cell Mito Stress Test Kit (Agilent), oligomycin, carbonyl cyanide-4 (trifluoromethoxy) phenylhydrazone (FCCP), and a mixture of rotenone and antimycin A were injected to final concentrations of 1–2 μM, 2 μM and 0.5 μM, respectively. OCR values were used to compute basal respiration, ATP production, proton leak, maximal respiration, spare respiratory capacity, and nonmitochondrial respiration. Calculations were performed using the XF Cell Mito Stress Test Report Generator from Seahorse Desktop Wave 2.6 software (Agilent).

Mitochondrial superoxide measurements

The level of mitochondrial superoxide was measured with MitoSOX™ Red mitochondrial superoxide indicator (Invitrogen). Cells were seeded in triplicate at the same density with the cell viability assay in 6-well plates, and stained with 5 μM MitoSOX reagent 24 hours after seeding according to the manufacturer's instructions. Fluorescence intensity for mitochondrial superoxide was determined with the BD Accuri C6 Flow Cytometer instrument.

In vivo BM studies

All animal work was performed in accordance with animal use protocol 00001597-RN01 under the auspices of the MDACC Institutional Animal Care and Use Committee (IACUC). 4–5 weeks old female SCID/beige mice were purchased from Envigo, and injected with 5×10^5 MDA-IBC3 cells into the tail veins as described previously [17]. IACS-10759 (5 mg/kg) was administered by oral gavage once a day starting 24 hours before cellular inoculation. Tumor development was monitored by weekly bioluminescence imaging (BLI) using the IVIS-200 imaging system from Xenogen. 96 days after injection, all mice were sacrificed and their brains were removed under sterile conditions. Brain metastatic lesions were then localized by ex vivo BLI. Brains were subsequently fixed in formalin for 24 hours, paraffin embedded, sectioned and stained with hematoxylin and eosin for histological analysis. Size and number of brain metastatic lesions were determined by a board-certified Neuropathologist (J.T.H.).

Isolation of BM derivative cell lines

To generate BM derivatives, two SCID/beige mice were subjected to tail vein injection with MDA-IBC3 as described above. Brain metastatic lesions were resected based on ex vivo BLI 100 days after inoculation. BM tissues were minced and placed in culture medium for MDA-IBC3 cells supplemented with 0.125% collagenase III and 0.1% hyaluronidase (both from STEMCELL Technologies). Cells were then incubated at room temperature for 5 hours, briefly centrifuged, resuspended in 0.25% trypsin, incubated for 15 min at 37 °C, and passed through a 40- μ m filter. Cells were resuspended in culture medium and grown to confluence on a 10-cm dish. GFP+ cells were sorted using a BD FACSAria Fusion (BD Biosciences) and further cultured for in vitro experiments.

Statistical analyses

Statistical analyses were performed with either GraphPad Prism 8.0, R (v3.5.0) or Microsoft Excel for Mac (v16.16.24). Mann-Whitney *U* tests were carried out to identify significance among cohorts for patient specimens, and treatment groups for in vivo studies. Two-sided Student's *t*-tests were performed to determine significance between parental and BM cell lines for in vitro studies. *P* values and hazard ratios in overall survival analysis with the Kaplan–Meier method were calculated by the log-rank test. Correlation coefficients (*R*) and two-tailed *P* values in linear regression analyses were calculated based on Pearson's correlation. The Benjamini–Hochberg method was applied to correct for multiple hypothesis testing. All statistically significant values are denoted as follows: **P* < 0.05, ***P* < 0.01, ****P* < 0.001 and *****P* < 0.0001.

Data availability

Data from whole-exome sequencing and mRNA-seq performed for this study have been deposited in the National Center for Biotechnology Information (NCBI) sequence read archive (SRA) under the BioProject ID PRJNA681304. Additional data from all platforms will be made available upon request.

Results

Genomic analyses reveal heterogeneous patterns of alterations in BMs

To identify recurrent molecular abnormalities driving BM, we assembled an experimental cohort (Table 1 and Supplementary Table 1, online resource) consisting of patient-matched BM and P/EM tissues derived from breast (*N* = 14), lung (*N* = 14), and renal cell (*N* = 7) carcinomas (RCC). All breast cancers were ductal adenocarcinomas and were composed of ER+ (*N* = 10), PR+ (*N* = 8), HER2-amplified (*N* = 5), and triple negative (*N* = 3) subtypes. Lung cancers were predominantly non-small cell variants, either adenocarcinoma (*N* = 9) or squamous carcinoma (*N* = 4), with one small cell carcinoma included. Finally, RCC samples were exclusively conventional clear-cell variant. Patient-matched normal samples were obtained in all cases, except for one RCC patient. We focused our study on patients for which frozen samples were available, facilitating the extraction of high-quality genomic DNA, mRNA and protein for downstream genomic, transcriptional and proteomic studies.

Biomaterial derived from our sample set enabled whole-exome sequencing, mRNA-seq, and RPPA profiling on largely overlapping tumor sets (Fig. 1a).

Whole-exome sequencing was employed to delineate the genomic landscape of P/EM-BM pairs. We found that the mutational profiles of our samples were largely reflective of cancer type. Overall mutational burdens fell within established rates for lung, breast and renal cell cancers [27], and did not differ significantly by P/EM versus BM status (Fig. 1b). Specific samples exhibited very high mutation rates, almost invariably in association with mutations in *POLE*, *POLD1*, and/or genes with established roles in DNA mismatch repair, arising in either the P/EM tumor or BM (Supplementary Fig. 1, online resource). These findings are consistent with hypermutation phenotypes arising stochastically, often in association with radiation and/or cytotoxic chemotherapy (Supplementary Fig. 1, online resource). We also investigated mutational signature profiles, which recent work confirmed can be effectively derived from exome sequencing across a range of cancers [35]. We found that mutational signatures, in general, did not vary markedly between P/EM and BM samples from the same cancer type, with the notable exception lung cancer. C to A transversions, known to be associated with smoking history [2], were prominent features in P/EM lung cancer samples but much less characteristic of patient-matched BM samples (Fig. 1c), likely reflecting alternative mechanisms of mutational acquisition operative in lung cancer BM.

Copy number abnormalities and mutations demonstrated characteristic patterns previously associated with the tumor types represented within our cohort [8–11], along with idiosyncratic evolution within P/EM-BM pairs (Fig. 1d, e). Well-established cancer-associated genes were involved in many cases, consistent with prior literature [7, 21]. Nevertheless, genomic alterations strongly and exclusively associated with BM were not evident, either within individual or across multiple histologies.

Proteomic profiling implicates canonical oncogenic pathway signaling as a BM driver across multiple cancer types

The lack of discrete genomic alterations associated with BM in our sample set prompted us to consider whether broad-based dysregulation of established oncogenic networks might characterize BM more generally. To address this possibility, we performed RPPA profiling on the majority of our sample set (Fig. 1a), obtaining quantitative information on a total of 443 protein and phospho-protein epitopes. Multidimensional scaling (MDS) analysis of RPPA data revealed that P/EM and BM samples largely clustered by tumor type, with significant overlap between the three represented histologies in terms of their global proteomic signatures (Fig. 2a). Nevertheless, pathway analyses using RPPA data revealed significant enrichment in BMs for canonical oncogenic signaling, including the PI3K-AKT, mTOR (mammalian target of rapamycin), and RAS-MAPK (mitogen-activated protein kinase) networks, extending across cancer type (Fig. 2b, c). Significant associations with PI3K-AKT, VEGF (vascular endothelial growth factor), chemokine, and ErbB signaling remained when lung, breast, and renal cell carcinomas were analyzed separately (Supplementary Fig. 2a–c, online resource). Several upregulated proteins were constituents in multiple pathways (Fig. 2d and Supplementary Table 2, online resource), indicative of well-established cross talk between oncogenic networks. These findings concur with prior

data from individual cancer types implicating canonical oncogenic signaling pathways, including the PI3K-AKT network, in BM [1, 12, 16].

BMs demonstrate evidence of decreased cellular immunity

We used mRNA-seq to interrogate the biological distinctions of BM relative to patient-matched P/EM samples. Echoing our RPPA findings, transcriptional profiling revealed that BMs largely cluster by MDS plotting with P/EM counterparts on the basis of histology (Fig. 3a), indicative of gene expression signatures that largely overlap with respective primary tumors. Nevertheless, analysis across cancer types demonstrated an array of significant correlations by GSEA. Consistent with earlier findings in melanoma [21], we observed significantly weaker associations for BM with a number of immune-regulatory and inflammatory signaling pathways compared to those exhibited by P/EM counterparts (Fig. 3b). These findings were recapitulated in a publicly available gene expression microarray dataset featuring primary breast cancer and non-patient-matched BMs (Supplementary Fig. 3, online resource) [29]. Our parallel proteomic analysis also revealed significant downregulation of several immune regulatory pathway protein constituents, despite the relatively poor representation of these networks on the RPPA platform (Fig. 3c).

To further define the microenvironmental distinctions underlying the transcriptional evidence of immune suppression in BM, we analyzed our mRNA-seq data using two computational algorithms: Estimation of Stromal and Immune Cells in Malignant Tumor Tissues Using Expression Data (ESTIMATE) and Microenvironmental Cell Populations (MCP)-counter [5, 49]. ESTIMATE delineates scores for stromal and immune compartments, while MCP-counter uses specific signatures to ascertain the relative abundance of the different immune cell populations. We documented significant decreases in stromal and immune scores ($P < 0.0001$ and $P = 0.0016$, respectively) by ESTIMATE, and in scores associated with multiple lymphoid and myeloid lineages by MCP-counter in BMs relative to P/EM tissues (Fig. 3d, e). These trends persisted, albeit with lower rates of statistical significance, when lung, breast, and renal cell cancers were examined independently (Supplementary Fig. 4a–f, online resource). To further evaluate immune cell compartments, we obtained formalin-fixed paraffin-embedded (FFPE) tissue sections of primary tumor ($N = 13$) and BM ($N = 20$) from lung, breast, and renal cell cancers—a sample set that extensively, though not completely, overlapped with our patient cohort used for multi-omic molecular profiling—and performed multiplexed immunofluorescence on the Vectra platform. This approach allowed us to spatially profile T lymphoid lineages in situ. We found significantly reduced CD3+ T cells in BM vs P/EM sections ($P = 0.0327$; Fig. 3f), consistent with transcriptional findings. Analogous trends for specific CD3+ T cell subsets were also seen but did not reach slightly statistical significance, likely reflecting an underpowering of our analysis for Vectra-based methodology (Supplementary Fig. 5, online resource).

Within our study cohort, high MCP-counter scores for specific T cells (T cells, CD8+ T cells, and cytotoxic lymphocytes) in BM were associated with increased overall survival from the time of craniotomy (Fig. 3g and Supplementary Fig. 6a, b, online resource). Interestingly, high T cell scores also correlated with increased programmed cell death protein

1 (PD-1, encoded by *PDCDI*) and programmed death-ligand 1 (PD-L1, encoded by *CD274*) transcriptional expression in BMs ($P=0.0030$ and $P=0.0285$, respectively), consistent with engagement of this key immunotherapy-related molecular network across tumor-microenvironmental interactions (Fig. 3h). T cell scores in BMs demonstrated no relationship to patient age, sex, and cancer type (Supplementary Fig. 7a–c, online resource). Taken together, these data point to immune suppression, particularly involving the cellular immunity, as a generalizable feature of BM across cancer type.

Gene expression signatures of OXPHOS characterize BM in multiple cancer types

Transcriptional data from BM samples exhibited enhanced associations by GSEA with multiple metabolic pathways relative to P/EM counterparts across breast, lung and renal cell cancers. This relationship was evident for both MSigDB hallmark and GO signatures, and prominently featured OXPHOS and related processes involving the mitochondrial respiratory chain complex (Fig. 4a, b). We also recapitulated these findings in the publicly available gene expression microarray dataset (Supplementary Fig. 8a, b, online resource) [29]. GSEA associations with the Hallmark_Oxidative_Phosphorylation were highly significant, even when breast, lung, and renal cell cancers were evaluated independently (all $P < 0.0001$; Fig. 4c).

We next scored all transcriptionally profiled samples by OXPHOS-index (OP-index) [21], to assess the distribution of OXPHOS activity across BM and P/EM tumors. We found that the average OP-index of BM samples was significantly higher than that of P/EM counterparts overall ($P < 0.0001$), despite considerable variability in absolute OP-index for both BM and P/EM tumor groups. Within patient-matched sets, 83.87% of BM samples exhibited increased OP-index relative to P/EM samples (Fig. 4d). The extent of OXPHOS activation with BM, as inferred by OP-index, demonstrated no associations with patient age, sex and cancer type (Supplementary Fig. 9a–c, online resource).

Transcriptional evidence of OXPHOS engagement in lung, breast, and renal cell cancer BM recapitulated earlier findings for melanoma [21]. In this prior work, increased OXPHOS was directly linked to the transcriptional coactivator peroxisome proliferator-activated receptor gamma coactivator 1-alpha (PGC-1 α , encoded by *PPARGC1A*), a master regulator of a variety of genes involved in cellular metabolism, and regulated by the melanoma lineage-specific transcription factor MITF [23, 43]. However, we did not observe significant upregulation of PGC-1 α transcript in our BM cohort ($P=0.3934$; Supplementary Fig. 10a, b, online resource), suggesting alternative mechanisms for OXPHOS activation in these cancer types. Interestingly, AKT-mediated phosphorylation of mitochondrial protein targets has been shown to stimulate OXPHOS in multiple cellular contexts [6, 14]. To evaluate this potential functionality in our sample set, we integrated transcriptional and RPPA data. This analysis detected a significant positive correlation between the Akt1 phospho-serine 473 epitope and OP-index within BM samples ($R=0.5452$; $P=0.0027$). mTORC1 signaling ($R=0.5325$; $P=0.0020$) and glycolysis ($R=0.6595$; $P < 0.0001$) ssGSEA signatures were also significantly associated with OXPHOS (Fig. 4e–h), and GSEA for BM samples dichotomized by Akt1 phospho-serine 473 levels revealed strong transcriptional links to several metabolic networks, including OXPHOS, suggestive of a generalized hypermetabolic

phenotype (Supplementary Fig. 11a, b, online resource). Taken together, these findings support enhanced OXPHOS as a general feature of BM, regardless of underlying histology, and provide mechanistic links to PI3K-AKT pathway activation.

BMs exhibit heightened oxidative metabolism and sensitivity to OXPHOS inhibition in vitro and in vivo

We next sought to functionally assess the importance of OXPHOS in BM using multiple independent experimental models. IACS-10759 is a small molecule OXPHOS inhibitor that targets mitochondrial complex I [21, 42, 51], and has been successfully employed in a variety of preclinical contexts. We applied IACS-10759 at increasing concentrations in vitro to breast cancer cell line derivatives with enhanced brain metastatic potential (MDA-MB-231-BR3 and BT474-BR3) along with their respective parental lines. The BR3 lines had previously been derived by three cycles of intracardiac injection in mice, each followed by BM harvest [45, 52]. In both cases, we found that the BR3 derivatives were more sensitive to OXPHOS inhibition (Fig. 5a, b). This reduced viability reflected, at least in part, increased apoptosis (Fig. 5c, d).

We then investigated whether BR3 derivatives have characteristics of enhanced oxidative metabolism relative to their respective parental lines as observed in clinical BM specimens. Seahorse analysis revealed that in both the MDA-MD-231 and BT474 contexts, BR3 derivatives exhibited significantly higher levels of oxidative metabolism relative to parental counterparts, most evident in increased maximal respiratory capacity ($P = 0.0047$ and $P = 0.0029$, respectively) and reserve capacity ($P = 0.0077$ and $P = 0.0070$, respectively). IACS-10759 appeared to almost completely abrogate oxidative metabolism in both parental and BR3 derivative cell lines (Fig. 5e–h and Supplementary Fig. 12a, b, online resource). Independent assessment of mitochondrial superoxide, an OXPHOS byproduct, also demonstrated enhanced oxidative metabolism in respective BR3 derivatives ($P < 0.0001$ and $P = 0.0002$, respectively; Fig. 5i, j). These results advance the notion that cancer cells selected for BM potential harbor higher levels of OXPHOS at baseline and are more sensitive to its inactivation.

To examine the impact of IACS-10759 for BM in vivo, we utilized the MDA-IBC3 cell line, originally derived from an inflammatory breast cancer, which robustly forms BMs in mice within a three-month time window following tail vein injection [17]. Two cohorts of SCID/beige mice ($N = 9$ each group) were inoculated with 5×10^5 MDA-IBC3 cells 24 hours after initiation of treatment with either vehicle or IACS-10759 (5 mg/kg by oral gavage; Fig. 6a). Daily administration of the compounds then continued until all mice were sacrificed at 96 days. We found that IACS-10759 treatment severely reduced BM formation, as assessed by ex vivo luminometry of luciferase-expressing MDA-IBC3 tumor nodules ($P = 0.0003$; Fig. 6b and Supplementary Fig. 13, online resource). Rigorous histopathological analysis confirmed these data, documenting much reduced BM number and cross-sectional area in IACS-10759-treated mice ($P = 0.0070$ and $P = 0.0057$, respectively; Fig. 6c–e). To further explore the impact of BM on cellular physiology, we isolated derivative cell lines, MDA-IBC3-BR1a and MDA-IBC3-BR1b, from BMs in two non-treated SCID/beige mice inoculated with parental MDA-IBC3 cells as well as our initial study (Supplementary Fig.

14, online resource). These lines were minimally passaged in culture and then assessed for sensitivity to IACS-10759. Similar to results for MDA-MB-231 and BT474 isogenic lines, we found that the MDA-IBC3 derivatives were more sensitive to OXPHOS inhibition than their parental counterpart (Fig. 6f). Moreover, both lines exhibited increased mitochondrial function relative to parental MDA-IBC3 cells when assessed by Seahorse analysis (Fig. 6g, h). These data underscore the functional relevance of OXPHOS to BM *in vivo*, and are reminiscent of similar findings recently reported in melanoma BM mouse models.

Discussion

BM represents a deadly, end-stage development for many of the most common systemic cancers, emphasizing its clinical relevance, particularly in the setting of continued improvements in the management of primary malignancies. That a restricted set of neoplasms exhibit a high frequency of BM underscores the likelihood of shared biological mechanisms driving the process at a fundamental level. Extensive genomic profiling has confirmed that distinct patterns of mutations and copy number alterations (CNAs) may drive clonal evolution in BM [7, 21, 39]. Of note, one recent study identified CNAs affecting *MYC*, *YAP1*, *MMP13*, and *CDKN2A* as enriched in lung adenocarcinoma BM relative to case-control primary tissue and promoting BM in lung adenocarcinoma models [39]. Taken together, however, these alterations only characterized a minority of lung adenocarcinoma BMs profiled and their involvement was not documented in other cancer types. Accordingly, alternative mechanisms with non-genomic foundations remain attractive candidates for molecular characterization and therapeutic targeting.

We first performed whole-exome sequencing on a cohort of lung, breast, and renal cell carcinomas—all cancers featuring high rates of BM—consisting of both BM and P/EM tissues. We found that BMs in our sample set exhibited heterogeneous patterns of genomic alterations falling within the spectrum of those associated with their respective tumor histologies. Moreover, while we observed mutations and CNAs distinguishing individual BMs from their patient-matched P/EM samples in many cases, we were unable to identify specific genomic alterations correlated with BM across tumor type. These findings echoed those of prior, large-scale studies whose analyses focused on narrower cross sections of tumor types [7, 21, 39].

To further probe shared biological mechanisms underlying BM, we integrated RNA-seq and RPPA profiling in our sample cohort, revealing a defined set of dysregulated physiological processes. First, we detected enhanced activity across an array of interconnected oncogenic signaling networks centered around the PI3K-AKT pathway. Prior work has implicated upregulated PI3K signaling in both melanoma and breast cancer BMs [1, 12, 16], and our results further support a central role in BM pathogenesis across tumor type. The precise BM-relevant functionalities engaged by enhanced PI3K signaling remain unclear. Beyond its established involvement in a wide range of oncogenic phenotypes, the pathway has also been extensively linked to cell survival, integrated stress responses, and metabolic regulation [22], all of which could be seen as advantageous to the complex process of BM. Associations with metabolic programming are particularly intriguing in light of our findings related to OXPHOS engagement.

Our analyses also documented evidence of decreased cellular immunity in BMs relative to patient-matched P/EM counterparts. Transcriptional profiling revealed significantly weaker associations with immune-regulatory and inflammatory signatures in BM, and subsequent processing through ESTIMATE and MCP-counter algorithms demonstrated reduced scores for multiple immune cell compartments. Multiplexed immunofluorescence confirmed significant reductions in T cell infiltration for BMs compared to P/EM tumors. These findings extend recent observations in melanoma and non-small cell lung cancer to multiple epithelial cancers characterized by frequent BM [21, 25], and their clinical relevance is underscored by significant associations between T cell signature strength in BM and patient survival. Moreover, our observed correlations between high T cell scores and increased PD-1/PD-L1 transcriptional expression in BMs have implications on the efficacy of immune checkpoint inhibition in this clinical context, as previous studies have linked CD8+ T cell and other immune cell infiltrates with responsiveness to anti-PD-1 immunotherapy [13, 41].

Gene expression profiling also revealed fundamental metabolic distinctions between BMs and P/EM tumors. Specifically, BMs exhibited enhanced associations with transcriptional signatures of OXPHOS and related biological processes involving the mitochondrial respiratory chain complex. Moreover, a refined metric of OXPHOS engagement, the OP-index, was increased in ~84% of BM samples relative to patient-matched P/EM counterparts. These findings suggest that the process of BM in neoplastic cells induces OXPHOS as an adaptive measure. Further supporting this conjecture, we found increased oxidative metabolism in brain metastatic derivatives of three distinct breast cancer cell lines. Taken together, these findings recapitulate those of prior work in melanoma [21], and raise the intriguing possibility that enhanced OXPHOS engagement represents a general feature of BM regardless of tumors type. That significant metabolic rewiring is required for effective BM is not entirely surprising, given the well-established nutritional constraints of the CNS microenvironment [24, 44]. Indeed, recent work has highlighted the central role played by serine biosynthesis in BMs derived from aggressive breast cancers [30]. The precise mechanisms driving upregulated OXPHOS in BM are unclear, and may vary by cancer type. As mentioned above, melanoma BMs appear to activate OXPHOS through upregulation of the transcriptional regulator PGC-1 α [21]. Our data indicate that alternative molecular networks are mobilized in breast, lung, and renal cell BMs, and may work in part through enhanced PI3K-AKT signaling. Prior work has delineated links between the PI3K-AKT pathway and cellular metabolism, including a specific role in mitochondrial function and OXPHOS [6, 14].

Pathogenic mechanisms operative in BM across multiple tumor histologies invite strategies for therapeutic targeting. We explored the possibility of OXPHOS inhibition as one such approach using both in vitro and in vivo experimental systems. Our findings demonstrated that the OXPHOS inhibitor IACS-10759 impaired oxidative metabolism and selectively targeted brain metastatic derivatives in three distinct cell lines. Moreover, IACS-10759 significantly hampered BM formation in a murine model of metastatic inflammatory breast cancer. Coupled with earlier work in melanoma [21], these data extend the efficacy profile of OXPHOS targeting to multiple tumor histologies of BM. Directly inhibiting a molecular pathway as foundational to human biology as OXPHOS may ultimately prove impractical on a clinical level [47]. Even in this setting, however, targeting the mechanism(s) by which

OXPHOS is engaged in BM remains a viable approach. Our findings, for instance, broadly implicate the PI3K-AKT pathway in OXPHOS activation for BM. Characterizing the specific molecular elements required for OXPHOS regulation within the extended PI3K-AKT signaling cascade and in other yet to be implicated molecular networks may prove fruitful as efforts to therapeutically combat BM continue to expand.

The limitations of this study derive from the absolute size of our sample cohort, despite its inclusion of the three most common brain metastatic cancer variants, and in vitro/vivo BM models from a limited cancer type. Definitive analysis of genomic alterations associated with BM was likely underpowered, and insufficient specimen number precluded more detailed study of molecular subtypes within each histological variant. Further confirmation and extension of our findings in larger tissue sets that include a broader spectrum of cancer types would be helpful. Similarly, our experimental validation of the central role of OXPHOS in BM biology was confined to in vitro and in vivo models of breast cancer. Given that enhanced oxidative metabolism appears to be a general feature of BM, regardless of histology, rigorously interrogating the impact of its functional inhibition over a wider range of BM models derived from multiple cancer types would be an essential pre-requisite to broad clinical translation.

In summary, we employ multi-omic molecular profiling, including transcriptional and proteomic analyses, to identify molecular features characterizing BM across tumor type. Our findings support the notion that a defined set of physiological parameters is required for effective BM, and that targeting these shared pathogenic mechanisms represents a promising strategy for therapeutic development.

Supplementary Material

Refer to Web version on PubMed Central for supplementary material.

Acknowledgments

We thank our patients and their families who provided samples for this research. We thank the Translational Molecular Pathology-Immunoprofiling lab (TMP-IL) at the Department Translational Molecular Pathology, University of Texas MD Anderson Cancer Center for multiplex immunofluorescence staining. This study was supported by NIH/National Cancer Institute Cancer Center Support Grant P30 CA016672 to the University of Texas MD Anderson Cancer Center (Advanced Technology Genomics Core Facility, RPPA Core Facility, Cytogenetics and Cell Authentication Core); MD Anderson Multidisciplinary Research Program; MD Anderson Multi-investigator Research Program; the American Cancer Society-Melanoma Research Alliance Team Award; a Taiho Pharmaceutical grant. J.T.H. is supported by the American Cancer Society and philanthropic contributions to the Melanoma Moon Shots Program of the University of Texas MD Anderson Cancer Center. M.A.D. is supported by the Dr. Miriam and Sheldon G. Adelson Medical Research Foundation, the AIM at Melanoma Foundation, Cancer Fighters of Houston, philanthropic contributions to the Melanoma Moon Shots Program of MD Anderson, and the Anne and John Mendelsohn Chair in Cancer Research. B.G.D. is supported by the Susan G. Komen Career Catalyst Research grant.

References

1. Adamo B, Deal AM, Burrows E, Geradts J, Hamilton E, Blackwell KL et al. (2011) Phosphatidylinositol 3-kinase pathway activation in breast cancer brain metastases. *Breast Cancer Res* 13:R125 10.1186/bcr3071 [PubMed: 22132754]

2. Alexandrov LB, Ju YS, Haase K, Van Loo P, Martincorena I, Nik-Zainal S et al. (2016) Mutational signatures associated with tobacco smoking in human cancer. *Science* 354:618–622. 10.1126/science.aag0299 [PubMed: 27811275]
3. Anders S, Pyl PT, Huber W (2015) HTSeq-A Python framework to work with high-throughput sequencing data. *Bioinformatics* 31:166–169. 10.1093/bioinformatics/btu638 [PubMed: 25260700]
4. Barnholtz-Sloan JS, Sloan AE, Davis FG, Vigneau FD, Lai P, Sawaya RE (2004) Incidence Proportions of Brain Metastases in Patients Diagnosed (1973 to 2001) in the Metropolitan Detroit Cancer Surveillance System. *J Clin Oncol* 22:2865–2872. 10.1200/JCO.2004.12.149 [PubMed: 15254054]
5. Becht E, Giraldo NA, Lacroix L, Buttard B, Elarouci N, Petitprez F et al. (2016) Estimating the population abundance of tissue-infiltrating immune and stromal cell populations using gene expression. *Genome Biol* 17:218 10.1186/s13059-016-1070-5 [PubMed: 27765066]
6. Bijur GN, Jope RS (2003) Rapid accumulation of Akt in mitochondria following phosphatidylinositol 3-kinase activation. *J Neurochem* 87:1427–1435. 10.1046/j.1471-4159.2003.02113.x [PubMed: 14713298]
7. Brastianos PK, Carter SL, Santagata S, Cahill DP, Taylor-Weiner A, Jones RT et al. (2015) Genomic characterization of brain metastases reveals branched evolution and potential therapeutic targets. *Cancer Discov* 5:1164–1177 10.1158/2159-8290.CD-15-0369 [PubMed: 26410082]
8. Cancer Genome Atlas Network (2012) Comprehensive molecular portraits of human breast tumours. *Nature* 490:61–70. 10.1038/nature11412 [PubMed: 23000897]
9. Cancer Genome Atlas Research Network (2012) Comprehensive genomic characterization of squamous cell lung cancers. *Nature* 489:519–525. 10.1038/nature11404 [PubMed: 22960745]
10. Cancer Genome Atlas Research Network (2013) Comprehensive molecular characterization of clear cell renal cell carcinoma. *Nature* 499:43–9. 10.1038/nature12222 [PubMed: 23792563]
11. Cancer Genome Atlas Research Network (2014) Comprehensive molecular profiling of lung adenocarcinoma. *Nature* 511:543–550. 10.1038/nature13385 [PubMed: 25079552]
12. Chen G, Chakravarti N, Aardalen K, Lazar AJ, Tetzlaff MT, Wubbenhorst B et al. (2014) Molecular profiling of patient-matched brain and extracranial melanoma metastases implicates the PI3K pathway as a therapeutic target. *Clin Cancer Res* 20:5537–5546. 10.1158/1078-0432.CCR-13-3003 [PubMed: 24803579]
13. Chen P-L, Roh W, Reuben A, Cooper ZA, Spencer CN, Prieto PA et al. (2016) Analysis of Immune Signatures in Longitudinal Tumor Samples Yields Insight into Biomarkers of Response and Mechanisms of Resistance to Immune Checkpoint Blockade. *Cancer Discov* 6:827–837. 10.1158/2159-8290.CD-15-1545 [PubMed: 27301722]
14. Chen Y-H, Su C-C, Deng W, Lock LF, Donovan PJ, Kayala MA, et al. (2019) Mitochondrial Akt Signaling Modulated Reprogramming of Somatic Cells. *Sci Rep* 9:9919 10.1038/s41598-019-46359-6 [PubMed: 31289326]
15. Cibulskis K, Lawrence MS, Carter SL, Sivachenko A, Jaffe D, Sougnez C et al. (2013) Sensitive detection of somatic point mutations in impure and heterogeneous cancer samples. *Nat Biotechnol* 31:213–219. 10.1038/nbt.2514 [PubMed: 23396013]
16. Davies MA, Stemke-Hale K, Lin E, Tellez C, Deng W, Gopal YN et al. (2009) Integrated Molecular and Clinical Analysis of AKT Activation in Metastatic Melanoma. *Clin Cancer Res* 15:7538–7546. 10.1158/1078-0432.CCR-09- [PubMed: 19996208]
17. Debeb BG, Lacerda L, Anfossi S, Diagaradjane P, Chu K, Bambhroliya A et al. (2016) miR-141-Mediated Regulation of Brain Metastasis From Breast Cancer. *J Natl Cancer Inst* 108:djw026 10.1093/jnci/djw026
18. Depristo MA, Banks E, Poplin R, Garimella KV, Maguire JR, Hartl C et al. (2011) A framework for variation discovery and genotyping using next-generation DNA sequencing data. *Nat Genet* 43:491–501. 10.1038/ng.806 [PubMed: 21478889]
19. Dobin A, Davis CA, Schlesinger F, Drenkow J, Zaleski C, Jha S et al. (2013) STAR: Ultrafast universal RNA-seq aligner. *Bioinformatics* 29:15–21. 10.1093/bioinformatics/bts635 [PubMed: 23104886]
20. Fidler IJ (2015) The Biology of Brain Metastasis: Challenges for Therapy. *Cancer J* 21:284–293. 10.1097/PPO.000000000000126 [PubMed: 26222080]

21. Fischer GM, Jalali A, Kircher DA, Lee WC, McQuade JL, Haydu LE et al. (2019) Molecular profiling reveals unique immune and metabolic features of melanoma brain metastases. *Cancer Discov* 9:628–645. 10.1158/2159-8290.CD-18-1489 [PubMed: 30787016]
22. Franke TF (2008) PI3K/Akt: getting it right matters. *Oncogene* 27:6473–6488. 10.1038/onc.2008.313 [PubMed: 18955974]
23. Haq R, Shoag J, Andreu-Perez P, Yokoyama S, Edelman H, Rowe GC et al. (2013) Oncogenic BRAF regulates oxidative metabolism via PGC1 α and MITF. *Cancer Cell* 23:302–315. 10.1016/j.ccr.2013.02.003 [PubMed: 23477830]
24. Katz R, Hamilton JA, Pownall HJ, Deckelbaum RJ, Hillard CJ, LeBoeuf RC et al. (2007) Brain Uptake and Utilization of Fatty Acids, Lipids & Lipoproteins: Recommendations for Future Research. *J Mol Neurosci* 33:146–150. 10.1007/s12031-007-0059-7 [PubMed: 17901559]
25. Kudo Y, Haymaker C, Zhang J, Reuben A, Duose DY, Fujimoto J et al. (2019) Suppressed immune microenvironment and repertoire in brain metastases from patients with resected non-small-cell lung cancer. *Ann Oncol* 30:1521–1530. 10.1093/annonc/mdz207 [PubMed: 31282941]
26. Langley RR, Fidler IJ (2011) The seed and soil hypothesis revisited—The role of tumor-stroma interactions in metastasis to different organs. *Int J Cancer* 128:2527–2535. 10.1002/ijc.26031 [PubMed: 21365651]
27. Lawrence MS, Stojanov P, Polak P, Kryukov GV, Cibulskis K, Sivachenko A et al. (2013) Mutational heterogeneity in cancer and the search for new cancer-associated genes. *Nature* 499:214–218. 10.1038/nature12213 [PubMed: 23770567]
28. Li H, Durbin R (2009) Fast and accurate short read alignment with Burrows-Wheeler transform. *Bioinformatics* 25:1754–1760. 10.1093/bioinformatics/btp324 [PubMed: 19451168]
29. McMullin RP, Wittner BS, Yang C, Denton-Schneider BR, Hicks D, Singavarapu R et al. (2014) A BRCA1 deficient-like signature is enriched in breast cancer brain metastases and predicts DNA damage-induced poly (ADP-ribose) polymerase inhibitor sensitivity. *Breast Cancer Res* 16:R25 10.1186/bcr3625 [PubMed: 24625110]
30. Ngo B, Kim E, Osorio-Vasquez V, Doll S, Bustraans S, Liang RJ et al. (2020) Limited Environmental Serine and Glycine Confer Brain Metastasis Sensitivity to PHGDH Inhibition. *Cancer Discov* 10:1352–1373. 10.1158/2159-8290.CD-19-1228 [PubMed: 32571778]
31. Niessner H, Forschner A, Klumpp B, Honegger JB, Witte M, Bornemann A et al. (2013) Targeting hyperactivation of the AKT survival pathway to overcome therapy resistance of melanoma brain metastases. *Cancer Med* 2:76–85. 10.1002/cam4.50 [PubMed: 24133630]
32. Olshen AB, Venkatraman ES, Lucito R, Wigler M (2004) Circular binary segmentation for the analysis of array-based DNA copy number data. *Biostatistics* 5:557–572. 10.1093/biostatistics/kxh008 [PubMed: 15475419]
33. Parra ER, Jiang M, Solis L, Mino B, Laberiano C, Hernandez S et al. (2020) Procedural Requirements and Recommendations for Multiplex Immunofluorescence Tyramide Signal Amplification Assays to Support Translational Oncology Studies. *Cancers (Basel)* 12:255 10.3390/cancers12020255
34. Parra ER, Uraoka N, Jiang M, Cook P, Gibbons D, Forget MA et al. (2017) Validation of multiplex immunofluorescence panels using multispectral microscopy for immune-profiling of formalin-fixed and paraffin-embedded human tumor tissues. *Sci Rep* 7:13380 10.1038/s41598-017-13942-8 [PubMed: 29042640]
35. Petljak M, Alexandrov LB, Brummel JS, Price S, Wedge DC, Grossmann S et al. (2019) Characterizing Mutational Signatures in Human Cancer Cell Lines Reveals Episodic APOBEC Mutagenesis. *Cell* 176:1282–1294.e20. 10.1016/j.cell.2019.02.012 [PubMed: 30849372]
36. Preusser M, Capper D, Ilhan-Mutlu A, Berghoff AS, Birner P, Bartsch R et al. (2012) Brain metastases: pathobiology and emerging targeted therapies. *Acta Neuropathol* 123:205–222. 10.1007/s00401-011-0933-9 [PubMed: 22212630]
37. Quail DF, Joyce JA (2017) The Microenvironmental Landscape of Brain Tumors. *Cancer Cell* 31:326–341. 10.1016/j.ccell.2017.02.009 [PubMed: 28292436]
38. Rimmer A, Phan H, Mathieson I, Iqbal Z, Twigg SRF, Wilkie AOM et al. (2014) Integrating mapping-, assembly- and haplotype-based approaches for calling variants in clinical sequencing applications. *Nat Genet* 46:912–918. 10.1038/ng.3036 [PubMed: 25017105]

39. Shih DJH, Nayyar N, Bihun I, Dagogo-Jack I, Gill CM, Aquilanti E et al. (2020) Genomic characterization of human brain metastases identifies drivers of metastatic lung adenocarcinoma. *Nat Genet* 52:371–377. 10.1038/s41588-020-0592-7 [PubMed: 32203465]
40. Thorvaldsdóttir H, Robinson JT, Mesirov JP (2013) Integrative Genomics Viewer (IGV): High-performance genomics data visualization and exploration. *Brief Bioinform* 14:178–192. 10.1093/bib/bbs017 [PubMed: 22517427]
41. Tumei PC, Harview CL, Yearley JH, Shintaku IP, Taylor EJM, Robert L et al. (2014) PD-1 blockade induces responses by inhibiting adaptive immune resistance. *Nature* 515:568–571. 10.1038/nature13954 [PubMed: 25428505]
42. Vangapandu HV, Alston B, Morse J, Ayres ML, Wierda WG, Keating MJ et al. (2018) Biological and metabolic effects of IACS-010759, an OxPhos inhibitor, on chronic lymphocytic leukemia cells. *Oncotarget* 9:24980–24991. 10.18632/oncotarget.25166 [PubMed: 29861847]
43. Vazquez F, Lim J-H, Chim H, Bhalla K, Girnun G, Pierce K et al. (2013) PGC1 α Expression Defines a Subset of Human Melanoma Tumors with Increased Mitochondrial Capacity and Resistance to Oxidative Stress. *Cancer Cell* 23:287–301. 10.1016/j.ccr.2012.11.020 [PubMed: 23416000]
44. Watts ME, Pocock R, Claudianos C (2018) Brain Energy and Oxygen Metabolism: Emerging Role in Normal Function and Disease. *Front Mol Neurosci* 11:216 10.3389/fnmol.2018.00216 [PubMed: 29988368]
45. Weil RJ, Palmieri DC, Bronder JL, Stark AM, Steeg PS (2005) Breast Cancer Metastasis to the Central Nervous System. *Am J Pathol* 167:913–920. 10.1016/S0002-9440(10)61180-7 [PubMed: 16192626]
46. Wen PY, Loeffler JS (1999) Management of Brain Metastases. *Oncology (Williston Park)* 13: 941–54, 957–61; discussion 961–2, 9. [PubMed: 10442342]
47. Yap TA, Rodon Ahnert J, Piha-Paul SA, Fu S, Janku F, Karp DD et al. (2019) Phase I trial of IACS-010759 (IACS), a potent, selective inhibitor of complex I of the mitochondrial electron transport chain, in patients (pts) with advanced solid tumors. *J Clin Oncol* 37:3014–3014. 10.1200/JCO.2019.37.15_suppl.3014
48. Ye K, Schulz MH, Long Q, Apweiler R, Ning Z (2009) Pindel: A pattern growth approach to detect break points of large deletions and medium sized insertions from paired-end short reads. *Bioinformatics* 25:2865–2871. 10.1093/bioinformatics/btp394 [PubMed: 19561018]
49. Yoshihara K, Shahmoradgoli M, Martínez E, Vegesna R, Kim H, Torres-Garcia W et al. (2013) Inferring tumour purity and stromal and immune cell admixture from expression data. *Nat Commun* 4:2612 10.1038/ncomms3612 [PubMed: 24113773]
50. Zhang J, Fujimoto J, Zhang J, Wedge DC, Song X, Zhang J et al. (2014) Intratumor heterogeneity in localized lung adenocarcinomas delineated by multiregion sequencing. *Science* 346:256–259. 10.1126/science.1256930 [PubMed: 25301631]
51. Zhang L, Yao Y, Zhang S, Liu Y, Guo H, Ahmed M et al. (2019) Metabolic reprogramming toward oxidative phosphorylation identifies a therapeutic target for mantle cell lymphoma. *Sci Transl Med* 11:eaau1167 10.1126/scitranslmed.aau1167 [PubMed: 31068440]
52. Zhang S, Huang W-C, Zhang L, Zhang C, Lowery FJ, Ding Z et al. (2013) Src Family Kinases as Novel Therapeutic Targets to Treat Breast Cancer Brain Metastases. *Cancer Res* 73:5764–5774. 10.1158/0008-5472.CAN-12-1803 [PubMed: 23913825]

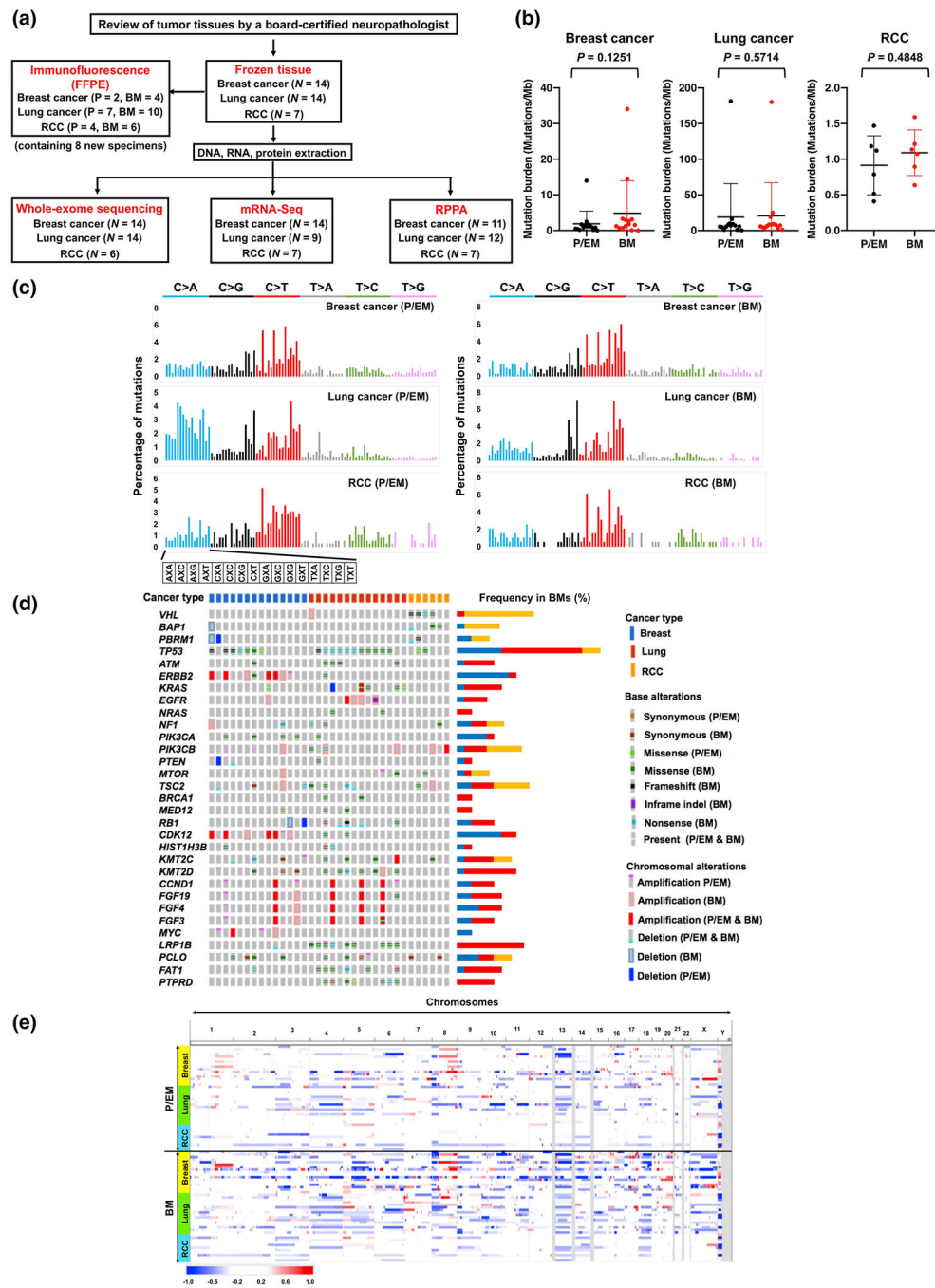


Fig. 1. Genomic characterization of BMs from breast, lung and renal cell carcinoma patients. **a** Schematic of multi-omic molecular analyses for BMs from multiple histologies. Number of patients with matched P/EM and BM tissues are shown. **b** Mutational burden for P/EMs and BMs from breast ($N = 14$), lung ($N = 14$) and renal cell ($N = 6$) carcinomas, respectively. P values were determined by Mann-Whitney U testing. Horizontal bars represent mean \pm SD. **c** Mutational signatures of P/EM and BM tissues. Signatures were displayed using 96 substitution classification divided into six categories according to single nucleotide

substitutions. Trinucleotide context in each category is arranged as indicated (bottom). X = C or T. 5 patients with hypermutation phenotypes were excluded in this analysis. **d** Landscape of somatic alterations in BM patients. Alteration type, frequency, BM vs P/EM status and cancer type are represented as indicated (right). **e** Landscape of CNAs in BM patients. CNA profiles are shown for P/EM (top) and BM (bottom) cohorts using Integrative Genomics Viewer

Author Manuscript

Author Manuscript

Author Manuscript

Author Manuscript

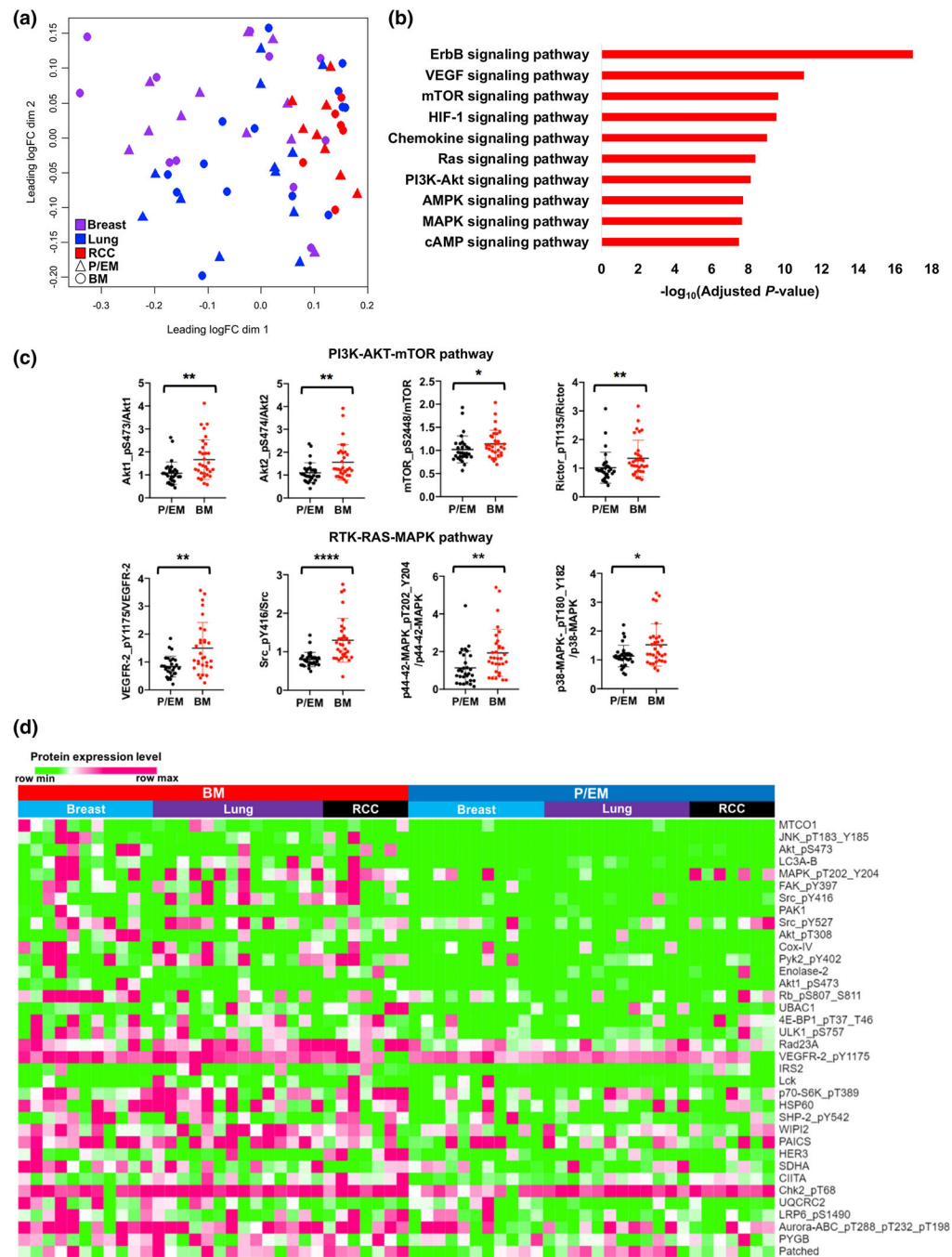


Fig. 2. Proteomic analysis reveals enhanced PI3K-AKT pathway signaling in BMs. **a** MDS plots of RPPA profiles from breast ($N=11$), lung ($N=12$) and renal cell ($N=7$) carcinomas (RCC). P/EM vs BM status and cancer types are shown with the colors and symbols. **b** Oncogenic signaling pathways activated in BMs. Significantly upregulated oncogenic pathways by RPPA in BMs ($N=32$) relative to P/EM ($N=30$) tumors. P values calculated by Fisher's exact test with Benjamini–Hochberg adjustment. **c** Representative constituents of PI3K-AKT-mTOR and RTK-RAS-MAPK pathways. Phosphorylated/total protein expression

values from RPPA for P/EM ($N=30$) and BM ($N=32$) cohorts. Horizontal bars represent mean \pm SD. * $P < 0.05$, ** $P < 0.01$, **** $P < 0.0001$, Mann-Whitney U testing. **d** Heatmap showing significantly ($P < 0.05$, Student's t -test) upregulated proteins in BMs ($N=32$) relative to P/EMs ($N=30$)

Author Manuscript

Author Manuscript

Author Manuscript

Author Manuscript

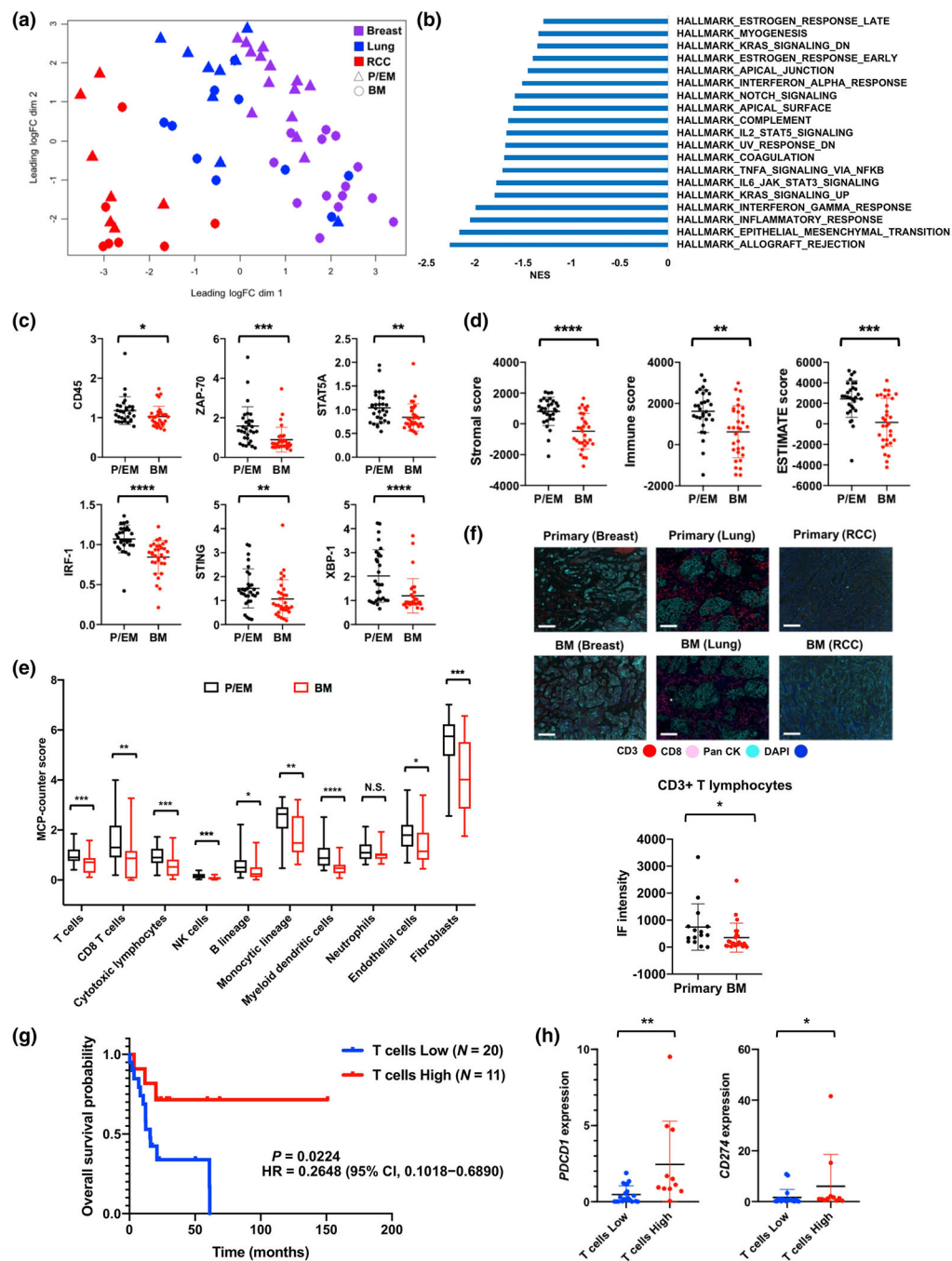


Fig. 3. Immunosuppression in BMs shared across multiple histologies. **a** MDS plots of transcriptional profiles from breast ($N = 14$), lung ($N = 9$) and renal cell ($N = 7$) carcinomas (RCC). P/EM vs BM status and cancer types are shown with the colors and symbols. **b** Significantly ($P < 0.05$ and FDR $q < 0.25$) downregulated pathways by GSEA in BMs ($N = 31$) relative to P/EMs ($N = 30$). NES, normalized enrichment score. **c** RPPA expression of representative immune-related proteins in P/EMs ($N = 30$) and BMs ($N = 32$). **d, e** Transcriptional signatures of immune cells. ESTIMATE (**d**) and MCP-counter (**e**) analyses

were performed for P/EMs ($N=30$) and BMs ($N=31$). Box and whisker plots indicate median and interquartile range (boxes), extending from minimum to maximum values (whiskers). **f** Representative immunofluorescence (IF) staining images (top) and quantification of CD3+ T lymphocytes (bottom) in primary tumors ($N=13$) and BMs ($N=20$) from breast, lung and renal cell carcinomas on the Vectra platform. Markers for CD3, CD8, pancytokeratin (Pan CK) and DAPI are shown by color as indicated. Scale bar, 100 μm . **g** Kaplan-Meier plots of overall survival from craniotomy for patients dichotomized by T cells status in BMs based on MCP-counter scores. P values and hazard ratios calculated by the log-rank test. **h** *PDCD1* and *CD274* expression in T cell low ($N=20$) and high ($N=11$) groups. **c, d, f, h** Horizontal bars represent mean \pm SD. * $P < 0.05$, ** $P < 0.01$, *** $P < 0.001$, **** $P < 0.0001$, Mann-Whitney U testing. N.S., not significant

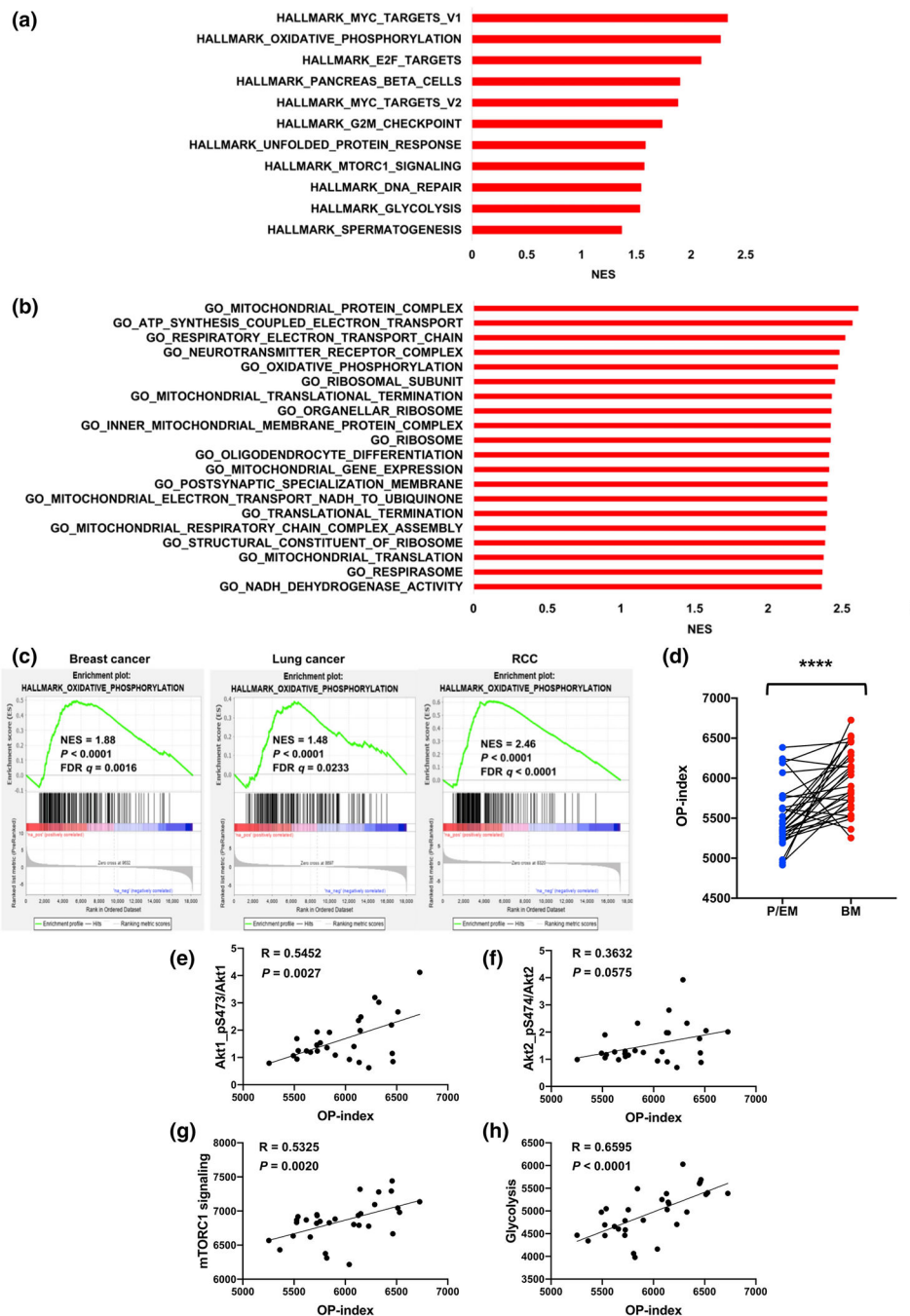


Fig. 4. Gene expression signatures of OXPHOS characterize BMs in multiple cancer types. **a, b** Significantly ($P < 0.05$ and FDR $q < 0.25$) upregulated MSigDB hallmark (**a**) and GO (**b**) gene sets in BMs ($N = 31$) relative to P/EMs ($N = 30$). **c** GSEA enrichment plots of Hallmark_Oxidative_Phosphorylation in breast ($N = 14$), lung ($N = 9$) and renal cell carcinoma (RCC) cohorts, respectively. NES, normalized enrichment score. **d** OP-index in P/EMs ($N = 30$) and BMs ($N = 31$). Horizontal bars represent mean \pm SD. **** $P < 0.0001$, Mann-Whitney U testing. **e-h** Association of OP-index with AKT-mTORC1 signaling.

Scatter plots show the correlation between OP-index and RPPA profiles of Akt1_pS473/Akt1 (**e**) and Akt2_pS474/Akt2 (**f**) ($N=30$), and ssGSEA signatures of mTORC1 signaling (**g**), glycolysis (**h**) ($N=31$) in BMs. Linear regression analyses are plotted. Correlation coefficients (R) and two-tailed P values calculated using Pearson's correlation

Author Manuscript

Author Manuscript

Author Manuscript

Author Manuscript

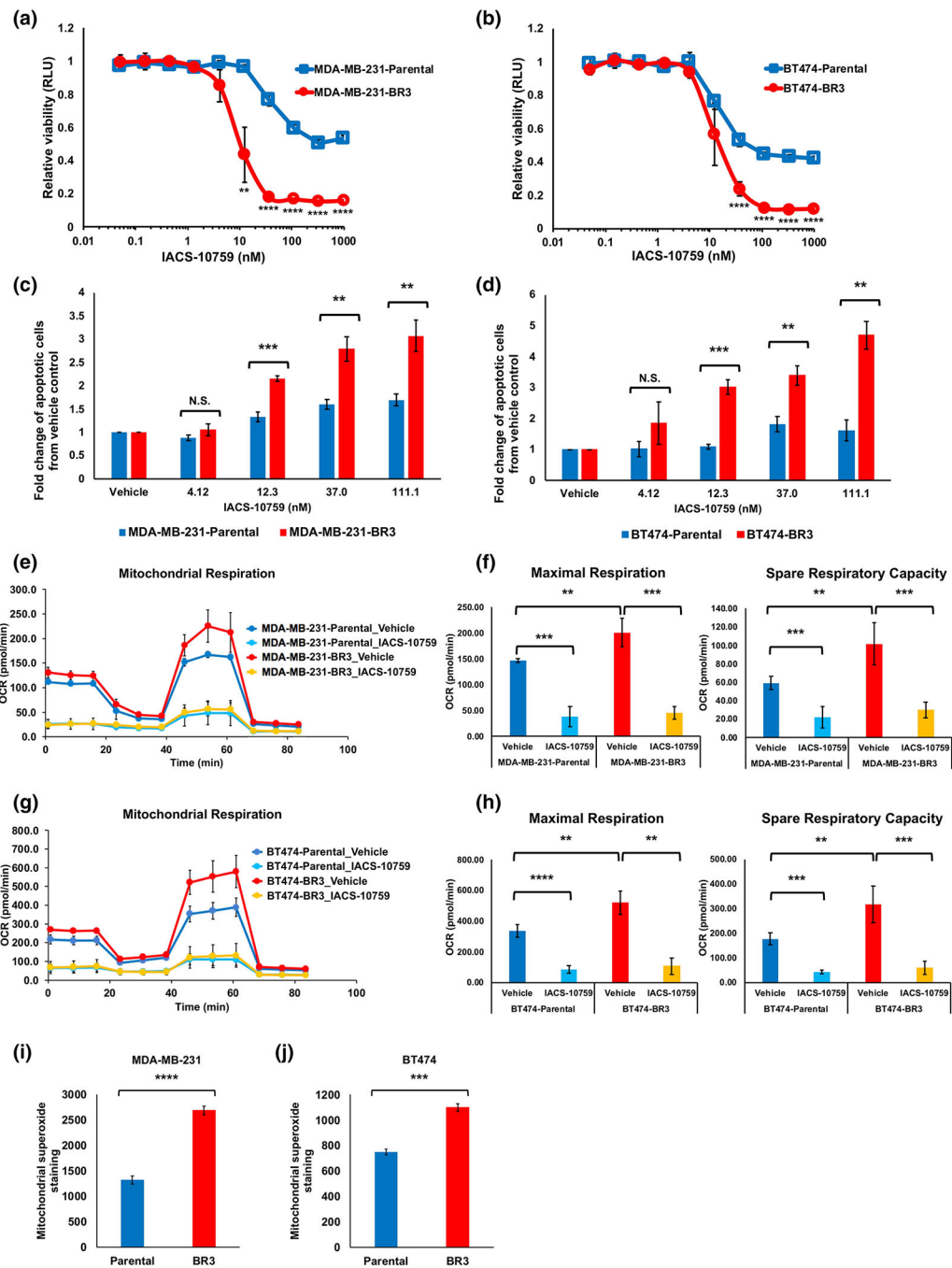


Fig. 5. Brain metastatic cell lines exhibit enhanced sensitivity to OXPHOS inhibition. **a, b** Cell viability of parental and BR3 derivatives of MDA-MB-231 (**a**) and BT474 (**b**) cell lines treated with IACS-10759 for 24 and 48 hours, respectively. Plots represent mean \pm SD from $N=4$ cultures. **c, d** Apoptosis assays for MDA-MB-231 (**c**) and BT474 (**d**) cell lines treated with IACS-10759 for 48 and 72 hours, respectively. Graphs represent mean \pm SD from $N=3$ cultures. **e, f** OCR in MDA-MB-231 cell lines treated with 40 nM IACS-10759 (**e**). Maximal respiration and spare respiratory capacity were computed based on the OCR trace (**f**).

Graphs represent mean \pm SD from $N=5$ cultures. **g, h** OCR in BT474 cell lines treated with 40 nM IACS-10759 (**g**). Maximal respiration and spare respiratory capacity were computed based on the OCR trace (**h**). Graphs represent mean \pm SD from $N=5$ cultures. **i, j** Mitochondrial superoxide in MDA-MB-231 (**i**) and BT474 (**j**) cell lines. Graphs represent mean \pm SD from $N=3$ cultures. All P values were computed using Student's t -test. ** $P < 0.01$, *** $P < 0.001$, **** $P < 0.0001$. N.S., not significant

Author Manuscript

Author Manuscript

Author Manuscript

Author Manuscript

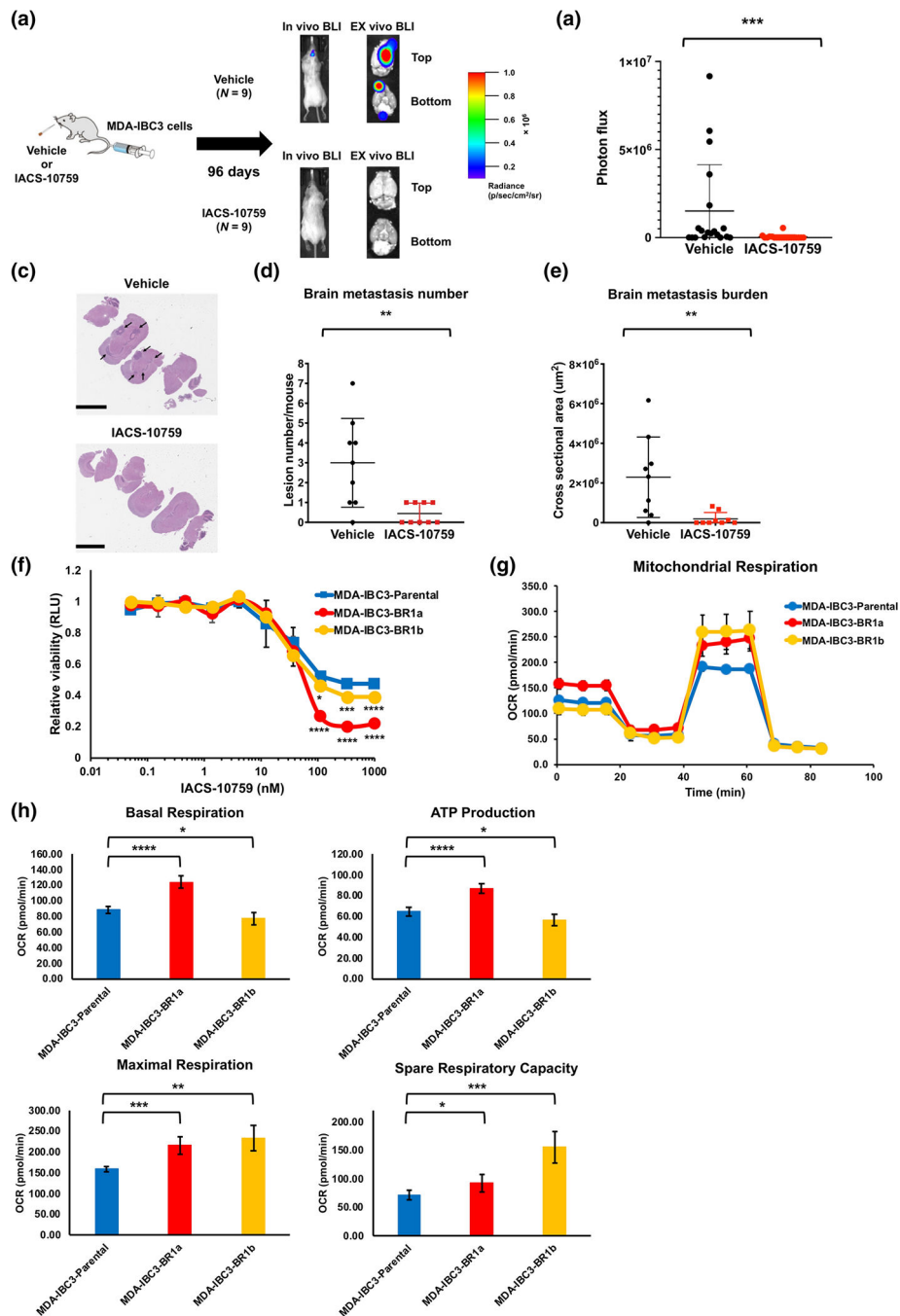


Fig. 6. OXPPOS inhibition impairs BM in vivo. **a** Schematic of in vivo murine modeling. SCID/beige mice ($N=9$ each group) were inoculated with MDA-IBC3 cells via tail vein injection. IACS-10759 (5mg/kg) was administered by oral gavage daily. Brains from all mice were removed 96 days post-inoculation. Representative in vivo and ex vivo bioluminescence images (BLI) are shown. **b** Quantification of BM BLI photon flux in vehicle and IACS-10759 treatment groups. Horizontal bars represent mean \pm SD. **c-e** Histopathological analysis of brain metastatic lesions. Representative hematoxylin and eosin (H&E) staining

images from vehicle (top) and IACS-10759 (bottom) treated groups (**c**). Black arrows indicate brain metastatic lesions. Scale bar, 5 mm. BM number (**d**) and cross-sectional area (**e**) per mouse were assessed in H&E staining slides by a Neuropathologist (J.T.H.). Horizontal bars represent mean \pm SD. **f** Cell viability of parental and BR derivatives (BR1a and BR1b) of MDA-IBC3 treated with IACS-10759 for 24 hours. Plots represent mean \pm SD from $N=4$ cultures. **g, h** OCR in MDA-IBC3 cell lines (**g**). Basal respiration, ATP production, maximal respiration and spare respiratory capacity were computed based on the OCR trace (**h**). Graphs represent mean \pm SD from $N=5$ cultures. Significance was assessed by Mann-Whitney U testing (**b, d, e**) or Student's t -test (**f, h**). * $P < 0.05$, ** $P < 0.01$, *** $P < 0.001$, **** $P < 0.0001$

Table 1

Clinical characteristics of BM patients

Primary cancer	Variable	Category	Number
Breast cancer (N= 14)	Sex	Male	1
		Female	13
	Histology	INVASIVE DUCTAL CARCINOMA	13
		DUCTAL CARCINOMA IN SITU (DCIS)	1
	Hormone status	ER+, PR+, HER2+	4
		ER+, PR+, HER2-	4
		ER+, PR-, HER2-	2
		ER-, PR-, HER2+	1
		ER-, PR-, HER2-	3
	Pathological grade of primary tumor	II	3
III		11	
Lung cancer (N= 14)	Sex	Male	7
		Female	7
	Histology	Adenocarcinoma	9
		Squamous cell carcinoma	4
		Small cell carcinoma	1
	Pathological grade of primary tumor	I	1
		II	3
		III	5
		IV	1
N/A		4	
Renal cell carcinoma (N= 7)	Sex	Male	3
		Female	4
	Histology	Clear cell	4
		Mixed clear cell	3
	Pathological grade of primary tumor	III	4
		IV	2
		Mixed II and IV	1

ER estrogen receptor, PR progesterone receptor, N/A not available.